

# Hyper-gap transparent conductor

Received: 12 November 2024

Accepted: 22 April 2025

Published online: 28 May 2025

 Check for updatesZhengran Wu<sup>1,2</sup>, Chunhong Li<sup>1</sup>, Xiaolei Hu<sup>1,2</sup>, Kun Chen<sup>1,2</sup>, Xiang Guo<sup>1,2</sup>, Yan Li<sup>1</sup> & Ling Lu<sup>1</sup>✉

An elusive conductor with perfect optical transparency holds revolutionary potential for fields such as optoelectronics and nanophotonics. Such a hypothetical metal would possess a spectral gap<sup>1,2</sup>—a ‘hyper-gap’—in its absorption spectrum, separating the intraband and interband absorptions, in which optical losses could vanish. Currently, this property is achievable only within the bandgap of insulators. However, realizing such a hyper-gap metal demands an exotic electronic structure in which the conducting bands have a bandwidth narrower than their energy separations from the remaining electronic states. Here we present such a hyper-gap in a family of organic metals—the Fabre charge-transfer salts<sup>3</sup>—through first-principles predictions coupled with both electrical and optical measurements. A transparent window, spanning from red to near-infrared wavelengths, is identified in bulk single crystals that remain transmissive over a thickness of 30  $\mu\text{m}$ . The corresponding absorption coefficient is the lowest among known stoichiometric metals, rivalling thin films of transparent conductive oxides. This finding introduces a path, beyond traditional doping strategies in insulators, to combine electronic conduction and optical transparency.

Optical transparency has been the privilege of insulators, such as glassware, optical fibres and clear plastics, essential for society. The ultra-high transparency in these materials is commonly understood through the absence of the density of states (DOS) in the bandgap (Fig. 1a). Since an optical transition involves both occupied and unoccupied electron states, a general condition for optical transparency is a spectral gap in the joint density of states (JDOS)—the convolution between the DOS values of both occupied and unoccupied electron states (Methods provides the definition). The zero JDOS inside the spectral gap fully suppresses optical absorption due to the lack of the simultaneous presence of initial and final electron states. In insulators, the JDOS gap coincides with the bandgap (Fig. 1b), leading to an effective lossless behaviour<sup>4</sup>. By contrast, regular metals are opaque because there is no energy gap in the DOS to induce a spectral gap in the JDOS (Fig. 1c,d), resulting in the continuous intraband absorption usually described by the Drude model. This broadband intraband absorption remains largely unchanged for modern transparent conductors, which are typically thin films of doped oxide insulators<sup>5</sup> (Fig. 1d,e). Doping shifts the Fermi level from inside the insulator gap to the bottom of the conduction band, enhancing conductivity at the cost of increasing absorption. Since the remaining energy gap exists only in the occupied electron

DOS (Fig. 1d; a similar concept of ‘gapped metal’<sup>6</sup>), it is insufficient to gap the JDOS and completely suppress absorption.

To fundamentally remove the optical absorption in metal, one needs to gap its JDOS by creating energy gaps in both its occupied and unoccupied electron DOS values below and above the Fermi level. As depicted in Fig. 1f,g, this means narrowing the metallic band and separating the conduction and valence bands, to the extent that the JDOS vanishes between the intraband and interband transitions. We dub this hypothetical JDOS gap in metal as the ‘hyper-gap’, in which the optical loss could be as low as that in the bandgap of insulators. Specifically, the hyper-gap criterion is  $E_{\text{intra}} < E_{\text{inter}} \equiv \min(E_{\text{inter}}^{\text{up}}, E_{\text{inter}}^{\text{down}})$ , where  $E_{\text{intra}}$  is the bandwidth of the metallic band and the interband onset  $E_{\text{inter}}$  takes a smaller value between  $E_{\text{inter}}^{\text{up}}$  and  $E_{\text{inter}}^{\text{down}}$ —the energies from the Fermi level to the conduction-band bottom and valence-band top, respectively. This hyper-gap metal was previously proposed to be an ideal transparent conductor<sup>1</sup> and a lossless metal for plasmonic metamaterials<sup>2</sup>, with paradigm-shifting potential. Unfortunately, there has been no clue of where to find this elusive metal with a seemingly unrealistic band structure<sup>7–9</sup>. Even a comprehensive high-throughput search yields false-positive results<sup>10</sup>, due to the instability of narrow-band metals, in all known inorganic compounds.

<sup>1</sup>Institute of Physics, Chinese Academy of Sciences/Beijing National Laboratory for Condensed Matter Physics, Beijing, China. <sup>2</sup>School of Physical Sciences, University of Chinese Academy of Sciences, Beijing, China. ✉e-mail: [linglu@iphy.ac.cn](mailto:linglu@iphy.ac.cn)

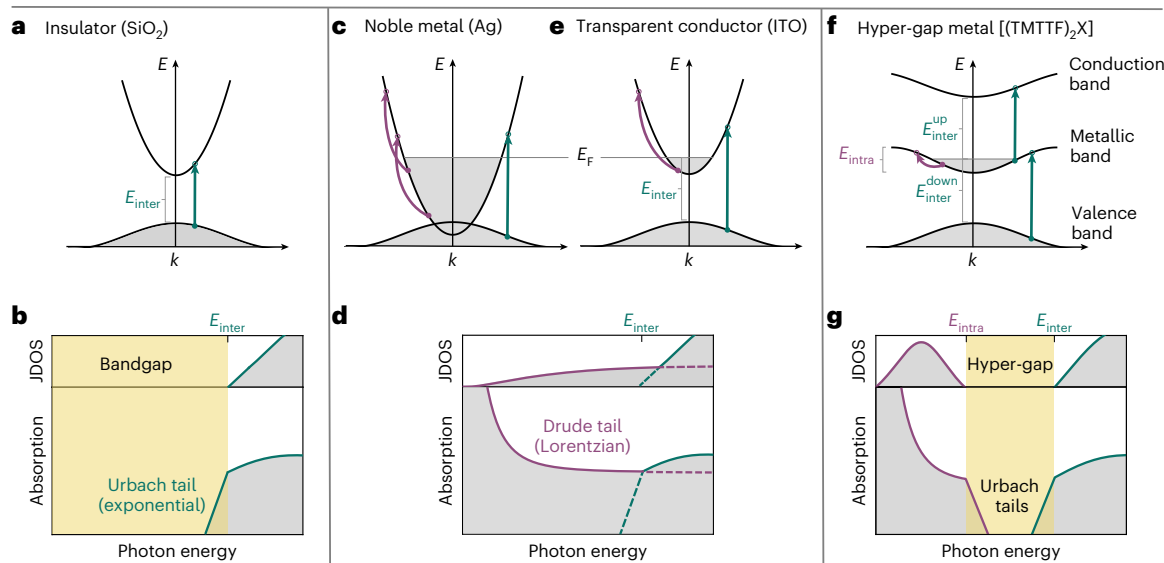


**Fig. 1 | Hyper-gap metal compared with insulator, noble metal and transparent conductor.** **a**, Band structure of an insulator (for example,  $\text{SiO}_2$ ). The green arrow represents the interband transition. The lower cut-off for interband transition occurs at energy  $E_{\text{inter}}$ . **b**, Schematics of JDOS (top) and the logarithm of the absorption coefficient (bottom) associated with the band structure in **a**. Theoretically, zero JDOS fully suppresses optical transitions. Experimentally, an exponential decay of absorption is universally observed from the band edge into the bandgap, known as the Urbach tail. **c, e**, Band structures of the noble metal (for example, Ag; **c**) and the transparent conductor

(for example, ITO; **e**). The purple arrows represent intraband transitions. **d**, JDOS and absorption associated with the band structures in **c** and **e**. The intraband absorption, commonly described by the Drude model, decays (in power laws) much slower than the exponential Urbach tail, limiting the lowest optical loss in both metals and transparent conductors. **f**, Band structure of a hyper-gap metal.  $E_{\text{intra}}$ , the bandwidth of the isolated metallic band, is the upper cut-off for intraband transitions. **g**, JDOS and absorption of the hyper-gap metal, whose intraband absorption will be cut off and exhibits a second Urbach tail in addition to the interband Urbach tail.

## Material prediction

In this Article, we shift our attention to organic conductors, where the bands are generally narrower and the correlated effects are weaker. We identify that the hyper-gap criteria can be satisfied in Fabre charge-transfer salts  $(\text{TMTTF})_2\text{X}$  (TMTTF, tetramethyltetrafulvalene;  $\text{C}_{10}\text{H}_{12}\text{S}_4$ ; X represents various monovalent anions like  $\text{SbF}_6^-$ ,  $\text{PF}_6^-$ ,  $\text{AsF}_6^-$  or  $\text{BF}_4^-$ ) that have been studied for its unconventional electronic properties and rich phase diagrams<sup>11</sup>. Since these quasi-one-dimensional metals are isostructural, we present the ab initio results of  $\text{X} = \text{SbF}_6^-$  in Fig. 2 as an example and compile the results for other anions in Extended Data Fig. 1. The crystal has a triclinic lattice, in which TMTTF molecules are separated in the crystallographic  $c$  axis by the  $\text{X}^-$  anions and arranged in a zig-zag pattern along the  $a$  axis ( $x$  axis)—the direction of electron conduction. The direction of current flow can be seen from the Fermi surface (Fig. 2a) and the band structure<sup>12</sup> (Fig. 2b), where the metallic band disperses in the  $x$  direction and is mostly dispersionless along the other directions. As shown from the partial DOS (Extended Data Fig. 2), the two metallic bands originate from the highest occupied molecular orbitals of the two TMTTF molecules in the unit cell, which transfer one electron to the  $\text{X}^-$  anion. The resulting metallic bands are quarter-filled with hole carriers (p type) with a density of  $1.5 \times 10^{21} \text{ cm}^{-3}$ . However, Hall measurements indicate that only 1% of this theoretical value of carrier density is effective for transport, since  $(\text{TMTTF})_2\text{X}$  is a Luttinger liquid—interacting electrons in one dimension<sup>13</sup>. More details are provided in Supplementary Note 3.

The isolated metallic (partially occupied) bands are adequately separated in energy compared with their own bandwidth, from both conduction (unoccupied) and valence (occupied) bands, revealing a hyper-gap in the JDOS spectrum (Fig. 2c). The bandwidth of the hyper-gap is as large as  $\sim 1 \text{ eV}$ , similar to the width of the metallic bands. A wide metallic band helps electric conduction and a wide hyper-gap helps optical transparency. The optical dielectric constants of  $(\text{TMTTF})_2\text{SbF}_6$  are computed in Fig. 2c. Due to the low crystalline symmetry of space group no. 2 ( $P\bar{1}$ ), all six complex components of the

permittivity tensor are present. We plot the two major in-plane components and the remaining are presented in Supplementary Fig. 2. The interband absorption ( $\epsilon_2^{xx}$ ) is much lower in the conductive  $x$  direction than those for the other directions ( $\epsilon_2^{yy}$  and  $\epsilon_2^{zz}$ ), because this is the out-of-plane direction of the planer TMTTF molecules in which the atoms are loosely spaced. Only  $\epsilon_1^{xx}$  is negative at low energy due to the quasi-one-dimensional electrical conductivity—a natural hyperbolic material<sup>14</sup>.

## Electrical measurements

Single crystals of  $(\text{TMTTF})_2\text{X}$  ( $\text{X} = \text{SbF}_6^-$ ,  $\text{PF}_6^-$ ,  $\text{AsF}_6^-$  and  $\text{BF}_4^-$ ) are grown by electrocrystallization<sup>15</sup> (Methods). The crystals are shiny rectangular plate-like structures with typical dimensions of  $5 \text{ mm} \times 0.2 \text{ mm} \times 0.04 \text{ mm}$  (Fig. 3a). The electrical resistivities of these molecular salts are measured along the metallic crystalline direction using the four-probe method (Supplementary Fig. 3). The temperature-dependent resistivity of  $(\text{TMTTF})_2\text{SbF}_6$  shows a metallic behaviour at room temperature, whose resistance decreases with temperature (Fig. 3b). A metal-to-Mott-insulator transition occurs at around 225 K due to charge localization, consistent with previous reports<sup>16–18</sup>. More transport properties are summarized in Supplementary Note 3. Although their room-temperature values of around  $10 \text{ S cm}^{-1}$  are much smaller than that of good metals ( $10^5 \text{ S cm}^{-1}$ ),  $(\text{TMTTF})_2\text{X}$  superconducts at low temperature ( $\sim 1 \text{ K}$ ) under pressure ( $\sim 30 \text{ kPa}$ ), whereas good metals such as gold, silver and copper have not been reported to be superconductors. Moreover, the optical absorptions of these organic conductors are much lower than that of silver<sup>19</sup>, which is widely regarded as the stable noble metal with the lowest optical loss.

## Optical characterizations

Closer examination of the thin-slab samples (Extended Data Fig. 3) under an optical microscope using back-illuminated white light indicates the transparent nature of these quasi-one-dimensional metals. As shown in Fig. 3c, the  $23\text{-}\mu\text{m}$ -thick crystal is transmissive in  $x$  polarization

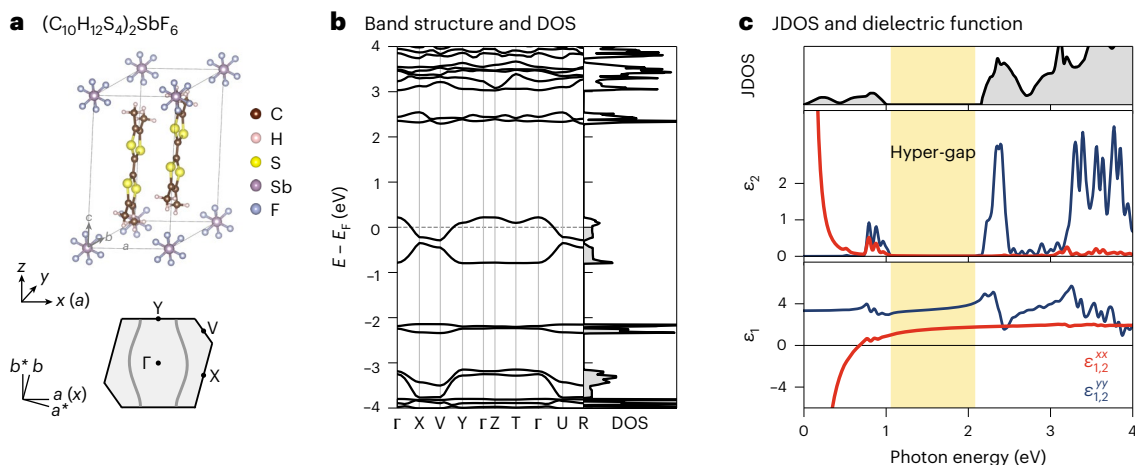


**Fig. 2 | Theoretical prediction of the hyper-gap conductor  $(\text{TMTTF})_2\text{SbF}_6$ .**

**a**, Crystal structure (top) and two-dimensional Brillouin zone in the  $k_z = 0$  plane (bottom).  $a$ ,  $b$  and  $c$  are the crystalline axes.  $x$ ,  $y$  and  $z$  are the orthogonal coordinates, where  $x$  is parallel to  $a$  and  $y$  is in the  $a$ - $b$  plane. The crystal structure is visualized using VESTA<sup>34</sup>. The two grey curves in the Brillouin zone represent

the Fermi surface.  $a^*$  and  $b^*$  are the reciprocal lattice vectors.  $a$  and  $b$  are projected in the  $a^*$ - $b^*$  plane. **b**, Band structure and DOS. The three-dimensional Brillouin zone is plotted in Supplementary Fig. 1. Capital letters ( $\Gamma$ ,  $X$ ,  $Y$ ) denote the high-symmetry points in the Brillouin zone. **c**, JDOS (top) and the complex anisotropic dielectric constants  $\varepsilon = \varepsilon_1 + i\varepsilon_2$  (bottom).

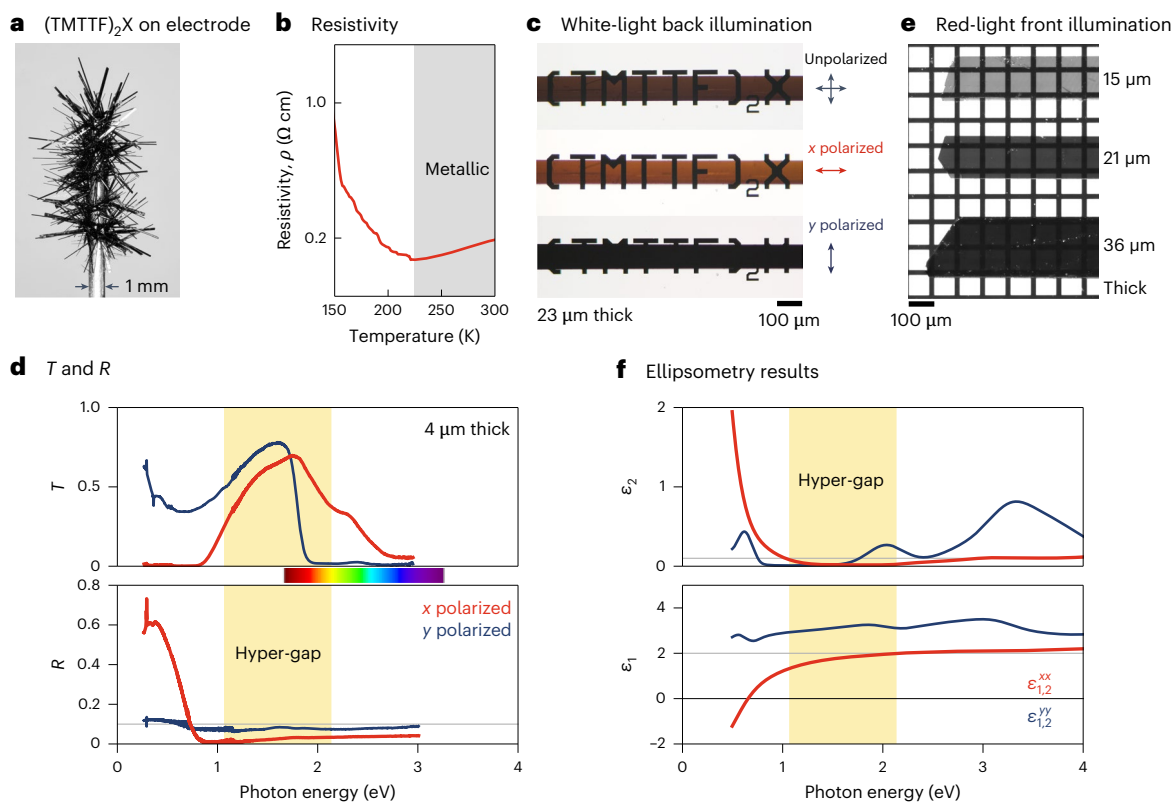


**Fig. 3 | Experimental results of  $(\text{TMTTF})_2\text{SbF}_6$ .** **a**, Optical images of the samples on an electrode. **b**, Temperature-dependent resistivity along the  $a$  axis. **c**, A 23- $\mu\text{m}$ -thick sample on opaque text under white-light back illumination. The top, middle and bottom photographs are illuminated by unpolarized,  $x$ -polarized and  $y$ -polarized light, respectively. **d**, Transmittance and reflectance of a 4- $\mu\text{m}$ -thick sample, with  $x$  and  $y$  polarizations of incident light. The rainbow colour bar is

presented to highlight the visible spectrum. **e**, Three samples with different thicknesses on a metal grid under red-light front illumination. **f**, Imaginary (top) and real (bottom) parts of the dielectric function obtained from ellipsometric measurements. The grey horizontal lines in **d** (bottom), **f** (top) mark the reference value of 0.1.

and is dark in  $y$  polarization. This polarizer-like behaviour is due to the anisotropic transmittance of the crystal in the visible spectra.

Transmittance spectra,  $T(\omega)$  (Fig. 3d), reveal the high transmittance peaks for both polarizations between 1 eV and 2 eV, overlapping the predicted hyper-gap highlighted by the yellow ribbon. The polarizer behaviour (Fig. 3c) is explained in the transmittance data, showing that

the  $x$ -polarization curve is much higher than that of  $y$  polarization in the visible spectrum (a complete polarization-dependent transmittance is presented in Extended Data Fig. 4). This is consistent with the theoretical prediction shown in Fig. 2c, where  $\varepsilon_2^{yy}$  is much larger than  $\varepsilon_2^{xx}$  above the hyper-gap. Below the hyper-gap, the transmittance of  $y$  polarization is higher, due to the insulator behaviour along the  $y$

direction. The dip appears at around 0.7 eV coinciding with the transition between the two metallic bands (Fig. 2b,c). Through the 4- $\mu\text{m}$ -thick  $(\text{TMTTF})_2\text{SbF}_6$  sample (Fig. 3d), the  $x$ -polarized transmittance peak is 70% at 708 nm and the  $y$ -polarization peak is 80% at 765 nm. The transmittance spectra of Fabre salts with other thicknesses and anions are presented in Supplementary Fig. 4. We then illuminate the samples with a red light-emitting diode of 704 nm (20 nm wide), which is around the peak transmittance of the material. In Fig. 3e, we see through single-crystal slabs as thick as 30  $\mu\text{m}$  to 40  $\mu\text{m}$ .

The reflectance spectra  $R(\omega)$  (Fig. 3d) also exhibit polarization-dependent anisotropy. The reflectance of  $y$ -polarized light remains nearly flat at  $\sim 10\%$  from 0.5 eV to 3 eV, a typical insulator behaviour. In the metallic direction of  $x$  polarization, a high plasma reflection appears at a low frequency ( $< 1$  eV) below the hyper-gap. The sharp resonance features below 0.5 eV in both  $R$  and  $T$  spectra are from the phonon modes that have been observed before<sup>20</sup>. Above 1 eV, the reflectance is consistently lower than 5% inside and above the hyper-gap. This low reflectance results from the low dielectric constant ( $\epsilon_1^{xx} < 2$ ) that we characterize with ellipsometry.

Ellipsometry measurements are performed to obtain the dielectric constants  $\epsilon(\omega)$  of these highly anisotropic crystals.  $\epsilon^{xx}$  and  $\epsilon^{yy}$  of  $(\text{TMTTF})_2\text{SbF}_6$  are plotted in Fig. 3e from 0.5 eV to 4 eV (Supplementary Fig. 5 shows the other components), which compares well with the theoretical results shown in Fig. 2c. The  $\epsilon_1^{xx}$  value turns negative below 0.6 eV, whereas  $\epsilon_1^{yy}$  remains positive—a typical hyperbolic material response<sup>21</sup>. Our measurement and fitting procedures on triclinic  $(\text{TMTTF})_2\text{X}$  are presented in Supplementary Note 4. We noted that ellipsometry is commonly used to determine the refractive indices of isotropic and uniaxial materials or films. The application of ellipsometry to the biaxial (orthorhombic, monoclinic and triclinic) materials is still under research<sup>22</sup>. Furthermore, the model-dependent ellipsometric result is not generally reliable for small absorption coefficients<sup>23</sup>, especially when the sample is highly anisotropic in this work. Consequently, for the loss analysis shown in Fig. 4, we extract the optical constants in the hyper-gap from the transmittance–reflection data, a standard way to obtain absorption coefficients for transparent materials (Supplementary Note 6).

## Loss analysis

The broadband material loss  $\epsilon_2(\omega)$  of  $(\text{TMTTF})_2\text{SbF}_6$  is plotted in the log scale in Fig. 4a, together with those of silver and indium tin oxide (ITO)—the low-loss natural metal and the standard transparent conductor, respectively. Across the whole energy range shown in Fig. 4a, the loss ( $\epsilon_2$ ) of  $(\text{TMTTF})_2\text{SbF}_6$  is over an order of magnitude smaller than that of silver<sup>24,25</sup>. Compared with ITO of a similar carrier density of  $\sim 10^{21} \text{ cm}^{-3}$  (doped), purchased from MTI Corporation,  $(\text{TMTTF})_2\text{SbF}_6$  has similar loss values whereas the wavelength of the loss minimum is redshifted, as defined by the hyper-gap. Interestingly,  $(\text{TMTTF})_2\text{SbF}_6$  has a lower plasma frequency, a lower refractive index and a lower material dispersion than those of ITO, around the visible wavelengths (Supplementary Fig. 8). These features are usually favoured for a transparent conductor, offering a potentially wider, higher and more uniform transmission. In addition, a low refractive index could be interesting for anti-reflective coatings and light extraction layers, high-contrast dielectric mirrors and waveguide claddings, as well as potentially near-zero-index materials<sup>26</sup>.

The intraband absorption of  $(\text{TMTTF})_2\text{SbF}_6$ ,  $\epsilon_2$  (Fig. 4a), does not follow the conventional Drude model that describes the low-frequency absorptions of most conductors, including silver and ITO. Instead, we find that the absorption coefficients  $\alpha(E)$  within the hyper-gap can be fitted by the Urbach equation<sup>4</sup>  $\alpha(E) \propto \exp(-|E - E_{\text{inter/intra}}|/E_U)$ , where  $E_U$  is the Urbach energy quantifying the steepness of the absorption onset at the band edges of insulators and semiconductors. As illustrated in Fig. 1, these observations are consistent with our expectation for a hyper-gap of zero JDOS, in which the Drude tail is replaced with the

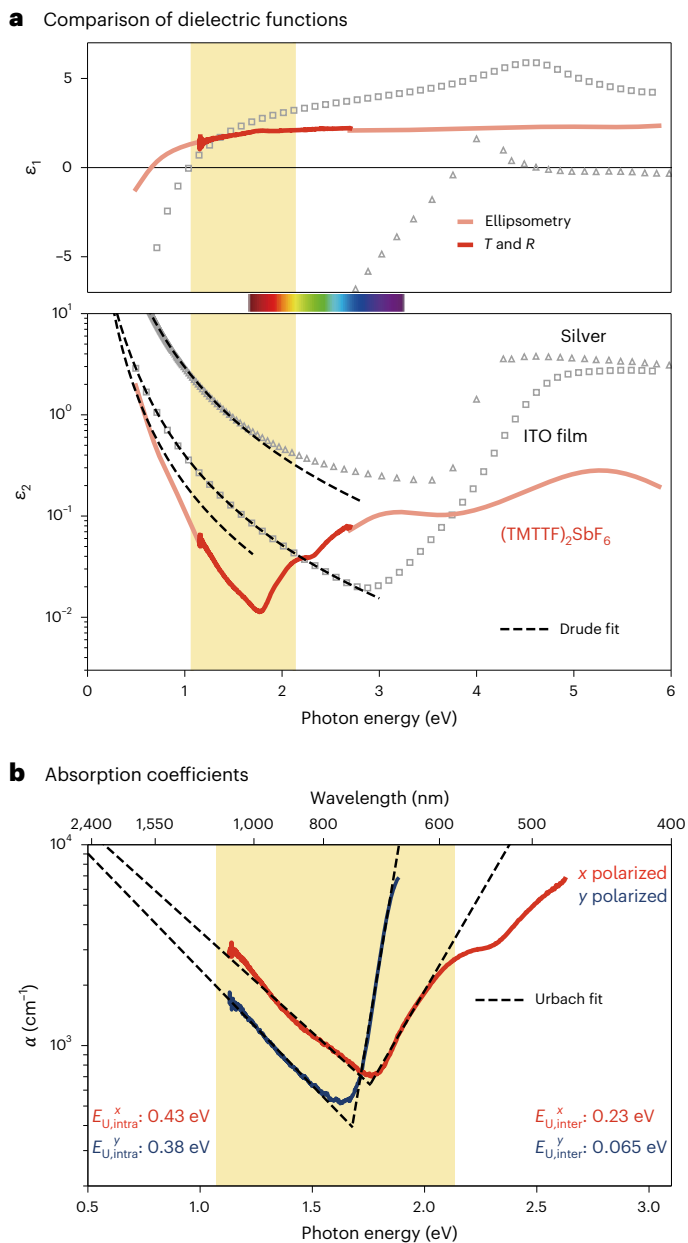


**Fig. 4 | Optical losses of  $(\text{TMTTF})_2\text{SbF}_6$ .** **a**, Comparison of the dielectric constants between  $(\text{TMTTF})_2\text{SbF}_6$ , silver and ITO film.  $\epsilon_2$  of  $(\text{TMTTF})_2\text{SbF}_6$  is the  $\epsilon_{xx}$  component, in which the data inside the low-loss hyper-gap (red) are obtained from the transmittance–reflection data (Fig. 3c) and the remaining data (light red) are obtained from the ellipsometry data (Fig. 3e). The  $\epsilon_2$  values of the three materials are fitted by the Drude model. **b**, Absorption coefficients of  $(\text{TMTTF})_2\text{SbF}_6$ , fitted by the Urbach rules with the Urbach energies listed.

Urbach tails from both intraband and interband edges. The fitted Urbach energies ( $E_{U,\text{inter/intra}}^{x/y}$ ) of both band edges (inter/intra) and both polarizations ( $x/y$ ) are listed in Fig. 4b. The Urbach energies of Fabre salts with other anions are presented in Extended Data Fig. 5 and Supplementary Note 3. The lowest Urbach energy  $E_{U,\text{inter}}^y = 65 \text{ meV}$  is similar to those of other crystalline organic insulators<sup>27,28</sup>. The large values of the other three Urbach energies (200–400 meV) are comparable to those reported in ITO<sup>29</sup>.

## Discussion

To the best of our knowledge, these Fabre salts have the lowest optical absorption among all known stoichiometric metals<sup>25,30</sup>. Apart from optimizing the crystal quality of  $(\text{TMTTF})_2\text{X}$ , a further reduction in

optical absorption involves finding new hyper-gap metals of either larger hyper-gap sizes or smaller Urbach energies. Fortunately, there are plenty of potential candidates to be explored in organic conductors, considering the vast number of carbon-based molecules. For example, as listed elsewhere<sup>31</sup>, the derivatives of TTF include TMTTF, HMTTF, BEDT-TTF, DBTTF and MDT-TTF. The sibling molecules of TTF include TSF, TTeF, TST, TTeT, TTA, TTN and TTP. The combination of the above donor molecules and the various acceptor ions X already forms a large family of compounds in which more hyper-gap candidates can be identified. Another relevant material class is the conductive metal–organic framework<sup>32</sup>.

A hyper-gap conductor, with further reduced absorption, can be highly interesting for a number of reasons. First, the stoichiometric hyper-gap metal could challenge the fundamental trade-off between the electrical and optical performances in transparent conducting oxides, in which higher doping decreases resistance but increases absorption. Second, the bulk hyper-gap metal can be made much thicker (>10 μm) than ITO films (~0.1 μm), whose thickness is limited by the deposition methods<sup>33</sup>. Thicker conductors have lower resistance, useful for applications that demand high current and minimal heat generation. Third, the hyper-gap metal, organic ones for instance, can be more cost-effective than noble metals and ITO due to indium scarcity. Fourth, the hyper-gap could be the solution to low-loss plasmonics when negative permittivity can be realized inside the hyper-gap by increasing the plasma frequency. This requires engineering the metallic band to achieve a smaller effective mass or a higher carrier concentration, by enhancing its Fermi velocity or boosting its DOS.

## Conclusion

We provide both theoretical and experimental evidence for the existence of the hyper-gap, in the molecular metal (TMTTF)<sub>2</sub>X, a much-anticipated theoretical proposal to eliminate optical absorption in metals. Several key questions are raised for future research, including how much further the electric conductivity can be increased and the optical absorption can be reduced in a hyper-gap metal, whether the negative permittivity can appear inside the hyper-gap<sup>19</sup> and if the mid-gap doping can be achieved to satisfy the hyper-gap criteria. We hope that our results would encourage further searches for hyper-gap conductors—a new material class in which the desired electrical and optical properties could coexist.

## Online content

Any methods, additional references, Nature Portfolio reporting summaries, source data, extended data, supplementary information, acknowledgements, peer review information; details of author contributions and competing interests; and statements of data and code availability are available at <https://doi.org/10.1038/s41563-025-02248-0>.

## References

- Medvedeva, J. E. & Freeman, A. J. Combining high conductivity with complete optical transparency: a band structure approach. *Europhys. Lett.* **69**, 583–587 (2005).
- Khurgin, J. B. & Sun, G. In search of the elusive lossless metal. *Appl. Phys. Lett.* **96**, 181102 (2010).
- Parkin, S. et al. Superconductivity in the organic charge transfer salts: (TMTSF)<sub>2</sub>X and (TMTTF)<sub>2</sub>X. *Mol. Cryst. Liq. Cryst.* **79**, 605–615 (1982).
- Mitra, S. S. & Bendow, B. (eds.) *Optical Properties of Highly Transparent Solids* (Springer, 1975).
- Ginley, D. S. (ed.) *Handbook of Transparent Conductors* (Springer, 2011).
- Malyi, O. I. & Zunger, A. False metals, real insulators, and degenerate gapped metals. *Appl. Phys. Rev.* **7**, 041310 (2020).
- Zhang, X., Zhang, L., Perkins, J. D. & Zunger, A. Intrinsic transparent conductors without doping. *Phys. Rev. Lett.* **115**, 176602 (2015).
- Gjerding, M. N., Pandey, M. & Thygesen, K. S. Band structure engineered layered metals for low-loss plasmonics. *Nat. Commun.* **8**, 15133 (2017).
- Wang, G. et al. Design of intrinsic transparent conductors from a synergetic effect of symmetry and spatial-distribution forbidden transitions. *Phys. Rev. Lett.* **134**, 036401 (2025).
- Hu, X. et al. High-throughput search for lossless metals. *Phys. Rev. Mater.* **6**, 065203 (2022).
- Jérome, D. The physics of organic superconductors. *Science* **252**, 1509–1514 (1991).
- Jacko, A. C. et al. Electronic properties of Fabre charge-transfer salts under various temperature and pressure conditions. *Phys. Rev. B* **87**, 155139 (2013).
- Korin-Hamzić, B., Tafra, E., Basletić, M., Hamzić, A. & Dressel, M. Conduction anisotropy and Hall effect in the organic conductor (TMTTF)<sub>2</sub>AsF<sub>6</sub>: evidence for Luttinger liquid behavior and charge ordering. *Phys. Rev. B* **73**, 115102 (2006).
- Korzeb, K., Gajc, M. & Pawlak, D. A. Compendium of natural hyperbolic materials. *Opt. Express* **23**, 25406–25424 (2015).
- Farges, J.-P. *Organic Conductors: Fundamentals and Applications* 138–140 (CRC Press, 1994).
- Dressel, M. et al. Charge and spin dynamics of TMTSF and TMTTF salts. *Synth. Met.* **120**, 719–720 (2001).
- Köhler, B., Rose, E., Dumm, M., Untereiner, G. & Dressel, M. Comprehensive transport study of anisotropy and ordering phenomena in quasi-one-dimensional (TMTTF)<sub>2</sub>X salts (X=PF<sub>6</sub>, AsF<sub>6</sub>, SbF<sub>6</sub>, BF<sub>4</sub>, ClO<sub>4</sub>, ReO<sub>4</sub>). *Phys. Rev. B* **84**, 035124 (2011).
- Itoi, M., Araki, C., Hedo, M., Uwatoko, Y. & Nakamura, T. Anomalous wide superconducting phase of one-dimensional organic conductor (TMTTF)<sub>2</sub>SbF<sub>6</sub>. *J. Phys. Soc. Jpn* **77**, 023701 (2008).
- Naik, G. V., Shalaev, V. M. & Boltasseva, A. Alternative plasmonic materials: beyond gold and silver. *Adv. Mater.* **25**, 3264–3294 (2013).
- Vescoli, V., Degiorgi, L., Starkey, K. P. & Montgomery, L. K. Anisotropy in the optical response of (TMTTF)<sub>2</sub>X (X=PF<sub>6</sub> and Br) Bechgaard salts. *Solid State Commun.* **111**, 507–512 (1999).
- Poddubny, A., Iorsh, I., Belov, P. & Kivshar, Y. Hyperbolic metamaterials. *Nat. Photon.* **7**, 948–957 (2013).
- Jellison, G. E., Podraza, N. J. & Shan, A. Ellipsometry: dielectric functions of anisotropic crystals and symmetry. *J. Opt. Soc. Am. A* **39**, 2225–2237 (2022).
- Fujiwara, H. *Spectroscopic Ellipsometry: Principles and Applications* 137–138 (John Wiley & Sons, 2007).
- Johnson, P. B. & Christy, R. W. Optical constants of the noble metals. *Phys. Rev. B* **6**, 4370–4379 (1972).
- Yang, H. U. et al. Optical dielectric function of silver. *Phys. Rev. B* **91**, 235137 (2015).
- Secondo, R., Khurgin, J. & Kinsey, N. Absorptive loss and band non-parabolicity as a physical origin of large nonlinearity in epsilon-near-zero materials. *Opt. Mater. Express* **10**, 1545–1560 (2020).
- Zhang, C. et al. Unraveling Urbach tail effects in high-performance organic photovoltaics: dynamic vs static disorder. *ACS Energy Lett.* **7**, 1971–1979 (2022).
- Ugur, E. et al. Life on the Urbach edge. *J. Phys. Chem. Lett.* **13**, 7702–7711 (2022).
- Khusayfan, N. M. & El-Nahass, M. M. Study of structure and electro-optical characteristics of indium tin oxide thin films. *Adv. Condens. Matter Phys.* **2013**, e408182 (2013).

30. Smith, N. V. Optical constants of sodium and potassium from 0.5 to 4.0 eV by split-beam ellipsometry. *Phys. Rev.* **183**, 634–644 (1969).
31. Graja, A. *Low-Dimensional Organic Conductors* (World Scientific, 1992).
32. Xie, L. S., Skorupskii, G. & Dinca, M. Electrically conductive metal–organic frameworks. *Chem. Rev.* **120**, 8536–8580 (2020).
33. Eshaghi, A. & Graeli, A. Optical and electrical properties of indium tin oxide (ITO) nanostructured thin films deposited on polycarbonate substrates ‘thickness effect’. *Optik* **125**, 1478–1481 (2014).
34. Momma, K. & Izumi, F. VESTA 3 for three-dimensional visualization of crystal, volumetric and morphology data. *J. Appl. Cryst.* **44**, 1272–1276 (2011).

**Publisher’s note** Springer Nature remains neutral with regard to jurisdictional claims in published maps and institutional affiliations.

Springer Nature or its licensor (e.g. a society or other partner) holds exclusive rights to this article under a publishing agreement with the author(s) or other rightsholder(s); author self-archiving of the accepted manuscript version of this article is solely governed by the terms of such publishing agreement and applicable law.

© The Author(s), under exclusive licence to Springer Nature Limited 2025

## Methods

### JDOS

The JDOS, in this Article, is defined as the correlation function between the DOS for filled (initial) and empty (final) electron states:  $\text{JDOS}(\hbar\omega) = \int_0^\omega \text{DOS}(\hbar\omega' - \hbar\omega)\text{DOS}(\hbar\omega')d\omega'$ , where  $\omega$  is the angular frequency and  $\hbar$  is reduced Planck constant. Here the Fermi level is at zero energy and the negative (positive) energy represents filled (empty) electron states. This simple definition includes contributions from both intraband and interband transitions, as well as both direct and indirect transitions. To have an ultralow optical absorption—effectively, lossless—the JDOS needs to vanish.

### Ab initio calculation

The electronic structures and optical properties of (TMTTF)<sub>2</sub>X are calculated using the Vienna Ab initio Simulation Package<sup>35</sup> with the hybrid functional HSE06 (ref. 36), where the lattice parameters are from the X-ray diffraction data on the crystals that we synthesize. Convergence is obtained with an energy cut-off of 500 eV. A  $\Gamma$ -centred Monkhorst–Pack mesh of  $6 \times 4 \times 4$   $k$  points in the first Brillouin zone are applied for computing the dielectric constants.  $\text{CSHIFT} = 0$  is applied in Fig. 2c to define the hyper-gap region in which  $\varepsilon_2 = 0$  ( $\varepsilon = \varepsilon_1 + i\varepsilon_2$ ). A JDOS-based Drude model<sup>10</sup> is used to compute the intraband absorption.

### Crystal growth

The single crystals of (TMTTF)<sub>2</sub>X (X = SbF<sub>6</sub>, PF<sub>6</sub>, AsF<sub>6</sub> or BF<sub>4</sub>) are grown by the electrocrystallization method<sup>15</sup>. TMTTF is placed on one side of an H-type glass cell, whereas the supporting electrolyte (KX; K, potassium) and the co-solvent (18-crown-6 ether) are on the other side. Solution (1,2-dichloroethane) is used on both sides. The oxidation of TMTTF takes place at the anode, where it is combined with anions provided by KX under a constant current of 1  $\mu\text{A}$ . Crystals are harvested in approximately 1 month.

### Sample characterizations

The temperature-dependent resistance is measured using a Quantum Design PPMS DynaCool system, with a constant current of 10  $\mu\text{A}$  and a cooling rate of 0.2 K  $\text{min}^{-1}$ . The electrical leads are 25- $\mu\text{m}$ -diameter gold wires glued on to the sample with silver paint.

The polarized transmittance and reflectance spectra are obtained at room temperature. For the low-photon-energy range (–0.27–1.15 eV), a Bruker HYPERION 2000 Fourier transform infrared microscope is used. For the high-photon-energy range (–1.15–2.95 eV), a custom-made optical setup is used.

Ellipsometric spectra are collected using a generalized spectroscopic ellipsometer over the infrared to ultraviolet (0.496–5.905 eV; RC2 J.A. Woollam) spectral range. The spectroscopic ellipsometer is equipped with a focusing probe attachment with an incident spot size of 150  $\mu\text{m}$ . The sample surface of the (001) plane is measured in two orientations: with the  $a$  axis aligned along and perpendicular to the  $x$  axis in the laboratory reference frame. At each sample orientation, five measurements are made with five incidence angles, namely, 63°, 66°, 69°, 72° and 75°. Supplementary Note 4 provides details of the modelling and analysis of the dielectric response.

### Absorption coefficients

The absorption coefficient  $\alpha$  is determined from the transmittance  $T$ , reflectance  $R$  and sample thickness  $d$ , with  $d$  measured using both

Bruker Dektak XT Profilometer and Bruker Contour GT-K1 Optical Profiler (Supplementary Fig. 9). The corresponding complex dielectric function  $\varepsilon_1 + i\varepsilon_2$  is calculated from the absorption coefficient  $\alpha$  and reflectance  $R$ . Supplementary Note 6 provides more details.

### Data availability

The data presented in the main text are available via Zenodo at <https://doi.org/10.5281/zenodo.15228102> (ref. 37). All other data are available from the corresponding author on reasonable request.

### References

- Hafner, J. Ab-initio simulations of materials using VASP: density-functional theory and beyond. *J. Comput. Chem.* **29**, 2044–2078 (2008).
- Heyd, J., Scuseria, G. E. & Ernzerhof, M. Hybrid functionals based on a screened Coulomb potential. *J. Chem. Phys.* **118**, 8207–8215 (2003).
- Wu, Z. Dataset: hyper-gap transparent conductor. *Zenodo* <https://doi.org/10.5281/zenodo.15228102> (2025).

### Acknowledgements

We thank X. Wang, S. Gao, T. Qian, G. Miao and B. Liu for helpful discussions. This work was supported by the Natural Science Foundation of China (12025409) and by the Chinese Academy of Sciences through the Project for Young Scientists in Basic Research (YSBR-O21), the Strategic Priority Research Program (XDB33000000) and the IOP-HKUST-Joint Laboratory for Wave Functional Materials Research. A portion of this work was carried out at the Synergetic Extreme Condition User Facility (SECUF) and the Laboratory of Microfabrication, IOP CAS.

### Author contributions

Z.W. performed the DFT calculations with the help of X.H.; conducted the crystal synthesis with the help of C.L.; conducted the electrical measurements; performed various optical measurements and analysis with the help of Y.L., X.G. and K.C.; and wrote the manuscript with L.L. who supervised the entire project.

### Competing interests

The authors declare no competing interests.

### Additional information

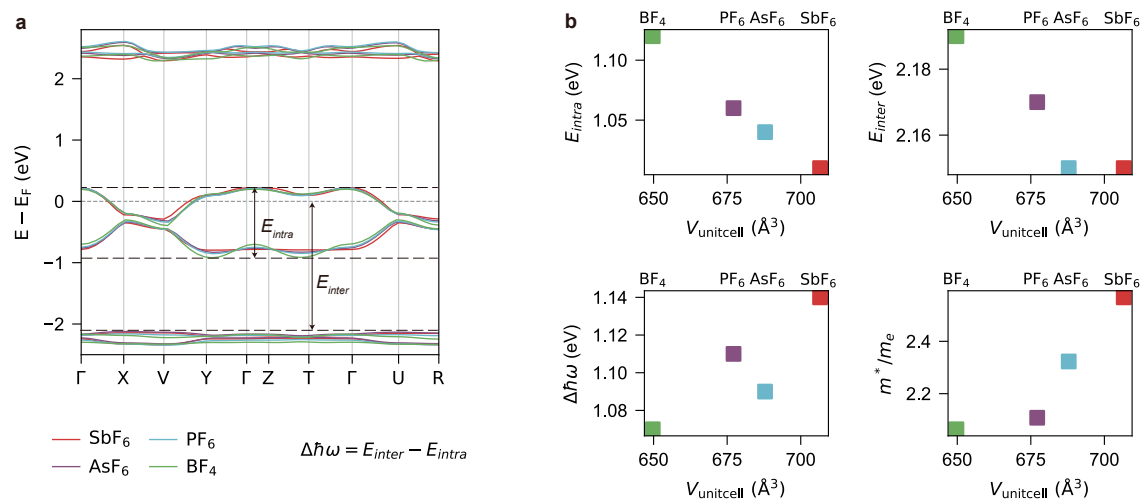
**Extended data** is available for this paper at <https://doi.org/10.1038/s41563-025-02248-0>.

**Supplementary information** The online version contains supplementary material available at <https://doi.org/10.1038/s41563-025-02248-0>.

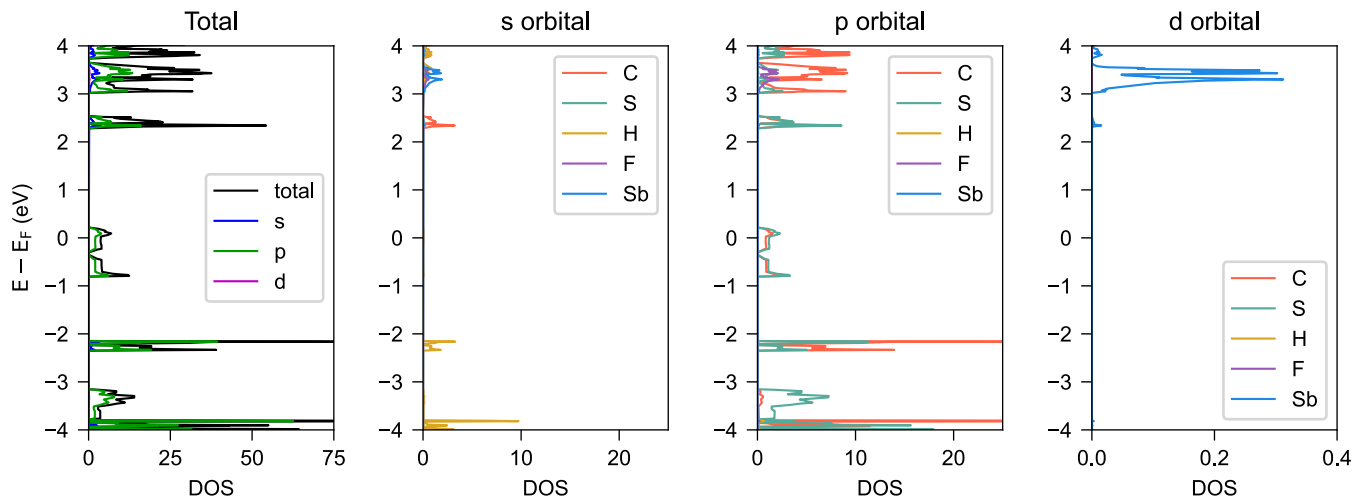
**Correspondence and requests for materials** should be addressed to Ling Lu.

**Peer review information** *Nature Materials* thanks Kazushi Kanoda and Jacob Khurgin for their contribution to the peer review of this work.

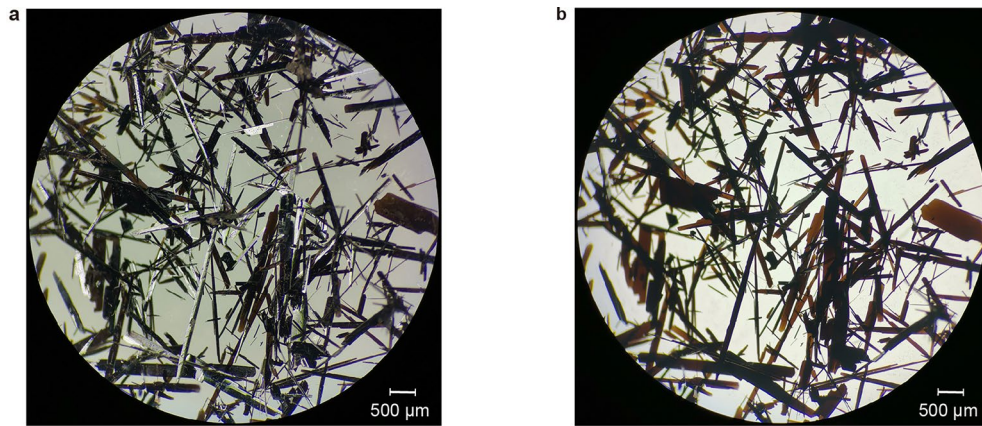
**Reprints and permissions information** is available at [www.nature.com/reprints](http://www.nature.com/reprints).



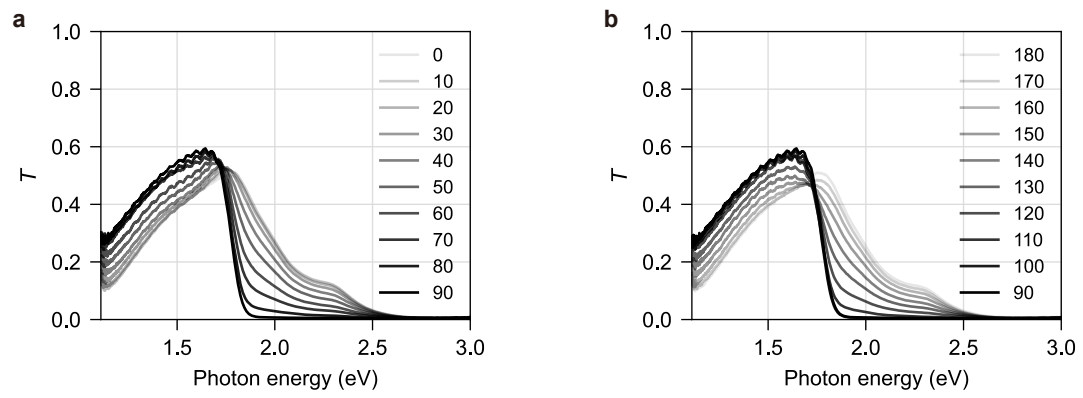
**Extended Data Fig. 1 | DFT results of  $(TMTTF)_2X$  with different anions  $X = SbF_6, PF_6, AsF_6$  and  $BF_4$ .** **a**, Band structure.  $E_{intra}$ : the bandwidth of the metallic band;  $E_{inter}$ : the distance from Fermi energy  $E_f$  to the band maximum of bands below -2 eV;  $\Delta \hbar\omega$ : the width of the hyper-gap. **b**, The dependence of  $E_{intra}$ ,  $E_{inter}$ ,  $\Delta \hbar\omega$ , and the effective mass  $m^*$  ( $m_e$  is the free electron mass) on different anions.



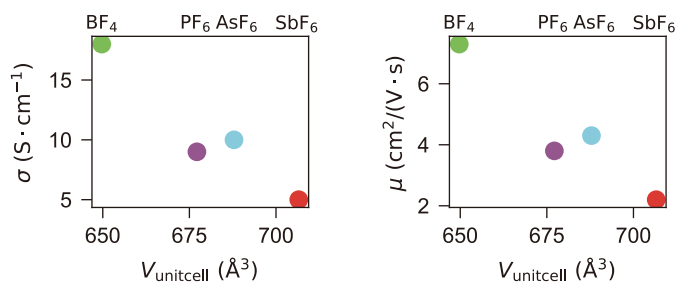
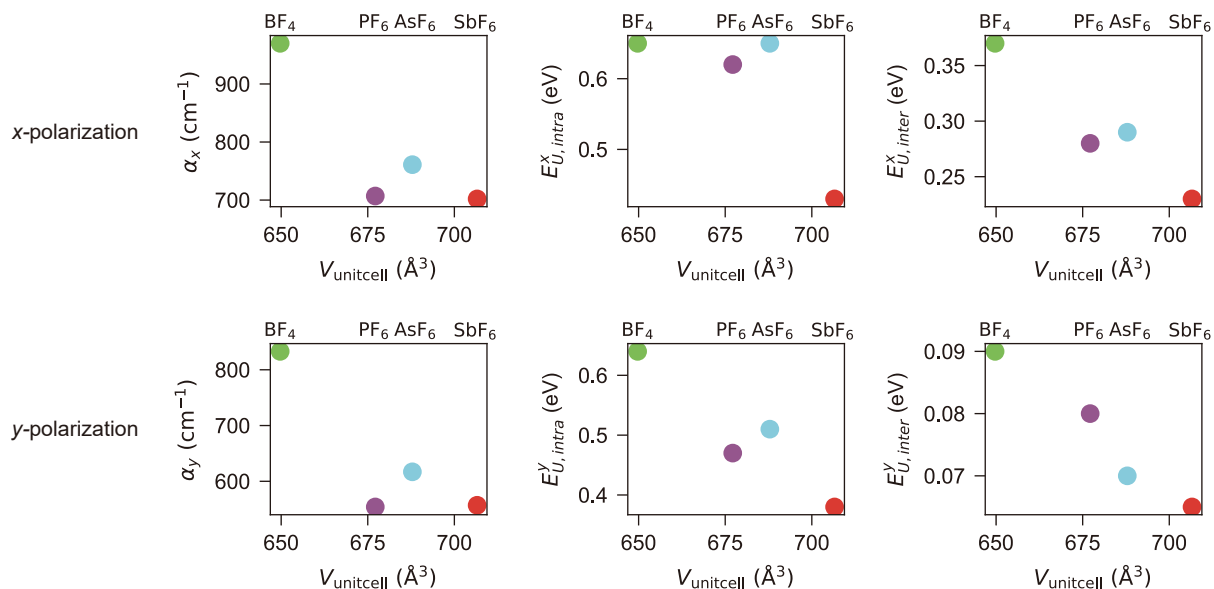
**Extended Data Fig. 2 | Density of states (DOS) and Partial density of states (PDOS) of  $(\text{TMTTF})_2\text{SbF}_6$ .** PDOS for  $s, p, d$  orbitals are contributed from different atoms.



**Extended Data Fig. 3 |  $(\text{TMTTF})_2\text{SbF}_6$  samples under the microscope. a,** Samples illuminated by white light from front side. **b,** Samples illuminated by white light from back side.



**Extended Data Fig. 4 | Polarization dependent transmittance of 6.5 μm-thick (TMTTF)<sub>2</sub>SbF<sub>6</sub>.** **a**, Transmittance spectra from 0° to 90° polarization. **b**, Transmittance spectra from 90° to 180° polarization.

**a** Electrical properties**b** Optical properties

**Extended Data Fig. 5 | Experimental electrical and optical properties of  $(\text{TMTTF})_2\text{X}$  with different anions  $\text{X} = \text{SbF}_6, \text{PF}_6, \text{AsF}_6$  and  $\text{BF}_4$  at room temperature. **a**,  $\sigma$ : conductivity along  $x$  direction;  $\mu$ : carrier mobility.  $\mu$  is derived from  $\sigma$  and calculated carrier density  $n$  using  $\mu = \sigma/(ne)$ . **b**, optical properties with**

$x$  and  $y$  polarized incident light, extracted from Supplementary Fig. 4.  $\alpha$ : lowest absorption coefficient;  $E_{U, \text{intra}}$  and  $E_{U, \text{inter}}$ : Urbach energies of the two tails (lower and higher energy sides) of the absorption spectra.